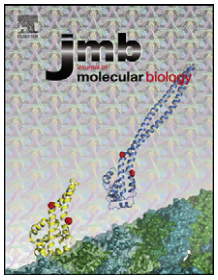

Molecular Interactions and Residues Involved in Force Generation in the T4 Viral DNA Packaging Motor

Amy D. Migliori [1], Douglas E. Smith [1] and Gaurav Arya [2]

*1 - **Department of Physics,** University of California at San Diego, La Jolla, CA 92093, USA*
*2 - **Department of NanoEngineering,** University of California at San Diego, La Jolla, CA 92093, USA*

Correspondence to Douglas E. Smith and Gaurav Arya: *des@physics.ucsd.edu; garya@ucsd.edu*
http://dx.doi.org/10.1016/j.jmb.2014.09.023
Edited by J. Johnson

Abstract

Many viruses utilize molecular motors to package their genomes into preformed capsids. A striking feature of these motors is their ability to generate large forces to drive DNA translocation against entropic, electrostatic, and bending forces resisting DNA confinement. A model based on recently resolved structures of the bacteriophage T4 motor protein gp17 suggests that this motor generates large forces by undergoing a conformational change from an extended to a compact state. This transition is proposed to be driven by electrostatic interactions between complementarily charged residues across the interface between the N- and C-terminal domains of gp17. Here we use atomistic molecular dynamics simulations to investigate in detail the molecular interactions and residues involved in such a compaction transition of gp17. We find that although electrostatic interactions between charged residues contribute significantly to the overall free energy change of compaction, interactions mediated by the uncharged residues are equally if not more important. We identify five charged residues and six uncharged residues at the interface that play a dominant role in the compaction transition and also reveal salt bridging, van der Waals, and solvent hydrogen-bonding interactions mediated by these residues in stabilizing the compact form of gp17. The formation of a salt bridge between Glu309 and Arg494 is found to be particularly crucial, consistent with experiments showing complete abrogation in packaging upon Glu309Lys mutation. The computed contributions of several other residues are also found to correlate well with single-molecule measurements of impairments in DNA translocation activity caused by site-directed mutations.

Introduction

Bacteriophages infect host cells by injecting their genome through the cell wall [1–3]. For successful delivery, the DNA must be stored at near-crystalline densities and under extremely high pressures within the phage capsid [4]. To achieve such high density packing, bacteriophages use powerful ATP-driven molecular motors that progressively push the DNA into the capsid against large resistive forces arising from DNA bending, electrostatic repulsion, and entropy loss [4–10]. In fact, these motors represent some of the most powerful molecular machines known to mankind, capable of generating forces in excess of 60 pN and packaging rates of up to 2000 bp/s [11–17]. Related motors package DNA in many animal viruses, including herpes viruses and adenoviruses. Single-molecule studies of several different phage DNA translocation motors have revealed their properties such as the motor step-size and kinetics [18–20], the nature of motor–DNA interactions [21], and the importance of conserved ATPase domain residues [22–24]. These studies have provided valuable information but have been limited in scope by the lack of availability of structural data needed to establish structure–function relationships. A detailed understanding of how viral DNA packaging motors are able to generate such high forces while packaging DNA at such rapid rates remains elusive and an active area of research.

The DNA packaging motor of bacteriophage T4 is one of the most powerful model systems for studying the molecular basis of force generation, as it represents the only motor for which the packaging

activity has been characterized by bulk and single-molecule assays and for which the atomic structure has been determined. Specifically, Sun *et al.* obtained a high-resolution X-ray structure of the T4 motor protein gp17 in its apo state (with empty ATP binding pocket) [25,26]. It was found that gp17 is organized into three globular domains: the N-terminal subdomains I and II and the C-terminal domain, which are connected by a short, loosely structured segment of residues referred to as the hinge. Concurrently, a low-resolution cryo-electron microscopy (cryo-EM) structure of the stalled motor in complex with the capsid was also reconstructed [25], revealing a pentameric arrangement of five gp17 units around the capsid portal. While differing conclusions have been reached in the literature regarding the orientation of gp17 subunits in the pentameric motor complex [27,28], direct structural data in which the X-ray structure of gp17 was fitted into the cryo-EM density map of the motor complex suggest that it is the N-terminal domain that binds to the portal. The fitting further revealed that the N- and C-terminal domains are separated by an additional ~7 Å relative to the corresponding separation in the X-ray structure, suggesting the presence of two distinct states of gp17: a compact state found in the X-ray structure and an extended state inferred from cryo-EM data. It was further observed that the compact form of gp17 forms a large interface between the N- and C-terminal domains containing apparently aligned clusters of complementarily charged residues on opposite faces. Based on these observations, a model for force generation was proposed [25] in which gp17 translocates DNA into the capsid in increments of ~2 bp by undergoing a transition from the extended to the compact state, putatively driven by electrostatic forces between complementarily charged residues across the interface separating the N- and C-terminal domains. ATP hydrolysis provides energy to cycle back to the extended state and reset the motor for the next translocation step.

Recently, we tested the abovementioned model of force generation by mutating selected charged residues at the interface between the N- and C-terminal domains that were suggested to be important for force generation [29]. We found that several of these mutations impaired both the packaging rate and the force-generating capability of the T4 motor. The extent of impairment for each mutation correlated well with computed differences in the free energy of compaction between wild type and mutant gp17, providing support for the proposed model of force generation. While the model proposes ion-pairing interactions across the interface as the driving force for the extended-to-compact transition, it is conceivable that polar uncharged (polar) and nonpolar uncharged (hydrophobic) residues are also likely involved in this transition. Indeed, if one defines the interface in terms of residues containing at least one atom within 5 Å of the opposite domain in the compact gp17 structure, then the interface contains a total of 46 residues of which 12 are charged, 11 are polar, and 23 are hydrophobic residues. That the interface buries ~1000 $Å^2$ of the two domains suggests that van der Waals (vdW) and hydrophobic forces could also play a role in stabilizing the compact state of gp17.

In this study, we investigate the molecular basis of force generation in gp17 by using molecular dynamics (MD) simulations. This approach allows us to examine in detail the molecular interactions operating across the domain interface and to also quantify the contribution from each type of interaction and residue to the compaction transition. We find that, in addition to the proposed role of electrostatic interactions between charged residues, interactions mediated by uncharged residues contribute equally in not more to compaction. In particular, of the twelve charged residues originally proposed to form inter-domain ion pairs, we find that only five contribute favorably to the free energy of compaction by forming strong salt bridges across the interface, whereas the others serve to stabilize intra-domain secondary structural elements or are too distant to form favorable salt bridges. In addition, we find that one polar residue and five hydrophobic residues participate in compaction by forming an extensive network of vdW interactions with surrounding residues. In addition to salt bridges and vdW interactions, water-mediated hydrogen bonds also play a role in stabilizing the compact form of gp17. The computed contributions of interface residues to the overall free energy of compaction correlate well with experimentally measured impairments in motor activity caused by residue changes.

Results

Our aim is to dissect the importance of various molecular interactions in driving the extended-to-compact transition in gp17 (Fig. 1). To this end, we adapted the approach of molecular mechanics–generalized Born surface area (MM-GBSA) [30], which allows us to compute the overall free energy change ΔG_{EC} of this transition from explicit solvent, all-atom MD simulations in an efficient manner by approximating the solvation free energy using the generalized Born model. The free energy change is defined here as $\Delta G_{EC} = G_C - G_E$, where G_C and G_E are the free energies of the compact and extended states, respectively. Importantly, this method also provides us information on individual contributions to the free energy change arising from each type of intermolecular interaction and each amino acid residue, helping us to identify types of interactions and residues most crucial to the compaction

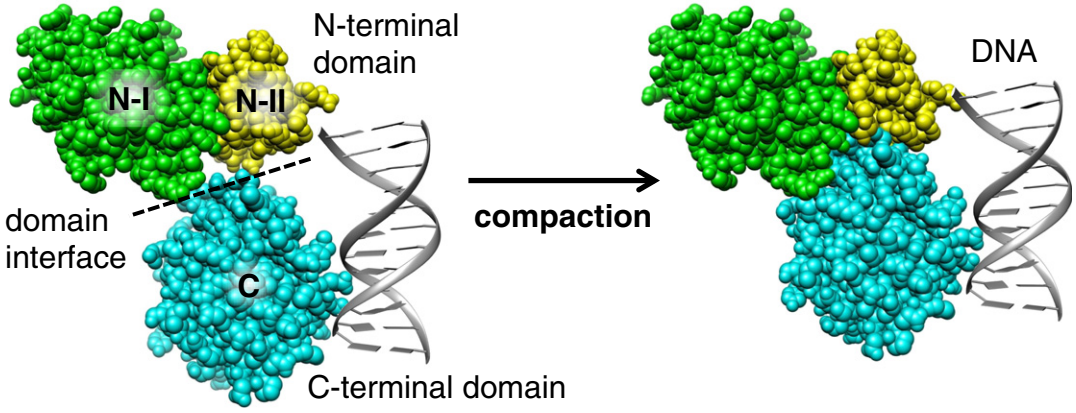

Fig. 1. Schematic of the proposed mechanism for DNA packaging in T4 bacteriophage involving conformational transition of gp17 from an extended to a compact state. The gp17 protein is shown as vdW spheres and the DNA, added for reference, is shown as smooth ribbons and slabs. Images were generated using the UCSF Chimera program.

transition. To understand why certain residues and interactions contribute to compaction while others do not, we carried out detailed structural analyses of the MD trajectories used for computing free energies. Specifically, we analyzed how gp17 compaction altered: the distances between complementarily charged pairs of residues across the N- and C-terminal domain interface, the network of vdW contacts made by interfacial residues, and the occupancy of solvent molecules around the interfacial residues. Note that, due to lack of a detailed structure for the multimeric complex, we study the compaction transition in a single gp17 subunit rather than the pentameric arrangement the motor assumes for packaging. It is not known whether neighboring subunits form strong contacts with each other, and it is unlikely that any contact would be mediated by the domain interface being studied here.

Polar and nonpolar interactions contribute equally to gp17 compaction

Our MM-GBSA calculations yield an overall free energy of compaction of $\Delta G_{EC} = -35.5 \pm 4.9$ kcal/mol. This value is slightly smaller in magnitude than that reported in our previous study [29], which included some artificial contributions from requirement of the MM-GBSA approach to divide the N- and C-terminal domains into two separate molecules at the hinge region. Previously, we showed that the strongly negative value of ΔG_{EC} is more than capable of generating the >60 pN forces measured in single-molecule packaging experiments on gp17. In the current study, we have further dissected this free energy of compaction into its different contributions to understand the origin of this highly favorable free energy of compaction.

Table 1 presents the breakdown of ΔG_{EC} in terms of changes in the molecular mechanics energy $\Delta E_{MM,EC}$ and solvation free energy $\Delta G_{solv,EC}$. The molecular mechanics energy has been further dissected into vdW energy $\Delta E_{vdW,EC}$, which accounts for changes in vdW interactions between the atoms of gp17 as it undergoes compaction, and electrostatic energy $\Delta E_{ele,EC}$, which accounts for changes in Coulombic interactions between charged atoms of gp17. Note that the Coulombic energy can arise from both charged and uncharged residues, as the atoms on uncharged residues also carry some partial charges in the force field. The solvation free energy $\Delta G_{solv,EC}$ has also been further dissected into polar $\Delta G_{pol,EC}$ and nonpolar solvation $\Delta G_{np,EC}$ contributions. The polar component $\Delta G_{pol,EC}$ accounts for solvent dielectric and salt screening effects not included in $\Delta E_{ele,EC}$, while the nonpolar component $\Delta G_{np,EC}$ accounts for vdW interactions between gp17 and the solvent and the free energy of cavity formation. For completeness, we also provide the corresponding contributions to the compact- and extended-state binding free energies $\Delta G_{bind,C}$ and $\Delta G_{bind,E}$ computed from MM-GBSA that were used to obtain the reported $\Delta G_{solv,EC}$ contributions.

Table 1. Interaction-level breakdown of the overall free energy of compaction ΔG_{EC} in kilocalories per mole (kcal/mol) as obtained from contributing terms of extended- and compact-state binding free energies

	Extended (i = E)	Compact (i = C)	Difference (i = EC)
$\Delta E_{ele,i}$	−245.9 (8.3)	−307.1 (8.0)	−61.3 (11.5)
$\Delta E_{vdW,i}$	−24.4 (4.5)	−42.6 (1.1)	−18.2 (4.7)
$\Delta E_{MM,i}$	−270.3 (9.6)	−349.8 (7.8)	−79.5 (12.4)
$\Delta G_{np,i}$	−7.0 (0.2)	−6.6 (0.1)	0.5 (0.2)
$\Delta G_{pol,i}$	282.8 (7.8)	326.2 (7.2)	43.5 (10.7)
$\Delta G_{solv,i}$	275.7 (7.8)	319.7 (7.2)	44.0 (10.7)
$\Delta G_{bind,i}$	**5.4 (4.8)**	**−30.1 (1.2)**	**−35.5 (4.9)**[a]

Numbers within parentheses represent standard errors in the reported values. A description of how these errors were estimated is provided in Materials and Methods.

[a] Computed ΔG_{EC} value.

Our analysis shows that the favorable free energy of compaction (ΔG_{EC}) originates from the highly favorable molecular mechanics energy ($\Delta E_{MM,EC}$ =−79.5 ± 12.4 kcal/mol) that more than compensates the unfavorable free energy of solvation ($\Delta G_{solv,EC}$ =44.0 ± 10.7 kcal/mol). The contributors to $\Delta E_{MM,EC}$ include the favorable vdW ($\Delta E_{vdW,EC}$ = −18.2 ±4.7 kcal/mol) and Coulombic interactions ($\Delta E_{ele,EC}$ =−61.27 ± 11.49 kcal/mol) between N- and C-terminal domains that obviously become stronger as the interacting groups get closer during gp17 compaction. The primary contributor to $\Delta G_{solv,EC}$ is the polar component of the solvation free energy ($\Delta G_{pol,EC}$ =43.5 ± 10.7 kcal/mol) arising from salt screening and dielectric effect whose magnitudes typically go hand in hand with the Coulombic energy. The contributions from nonpolar solvation ($\Delta G_{np,EC}$ = 0.5 ± 0.2 kcal/mol) are minimal, implying that the compact state of gp17 excludes only slightly more water molecules from the domain interface as compared to the extended state.

We next used the abovementioned energy breakdown to obtain the overall contribution from all polar $\Delta G_{tot\text{-}pol,EC}$ and nonpolar $\Delta G_{tot\text{-}np,EC}$ interactions. As discussed later, $\Delta G_{tot\text{-}pol,EC}$ provides a better measure of the role of electrostatic interactions in gp17 compaction than $\Delta E_{ele,EC}$. We find that the net polar contribution to ΔG_{EC} is −17.8 ± 15.7 kcal/mol while the net nonpolar energy contribution is −17.7 ± 4.7 kcal/mol. These calculations indicate that although polar interactions play an important role in driving the compaction transition in gp17, in agreement with the model of Sun *et al.* [25], nonpolar interactions across the interface arising from vdW contacts are equally important.

Free energy decomposition reveals residues that contribute significantly to compaction

To determine the residues most involved in gp17 compaction, we further decomposed the overall free energy ΔG_{EC} to obtain the contribution $\Delta G_{res,i}$ of each gp17 residue (*i* is the residue index) (Fig. 2a), where residues contributing large, negative $\Delta G_{res,i}$ would be expected to contribute strongly to

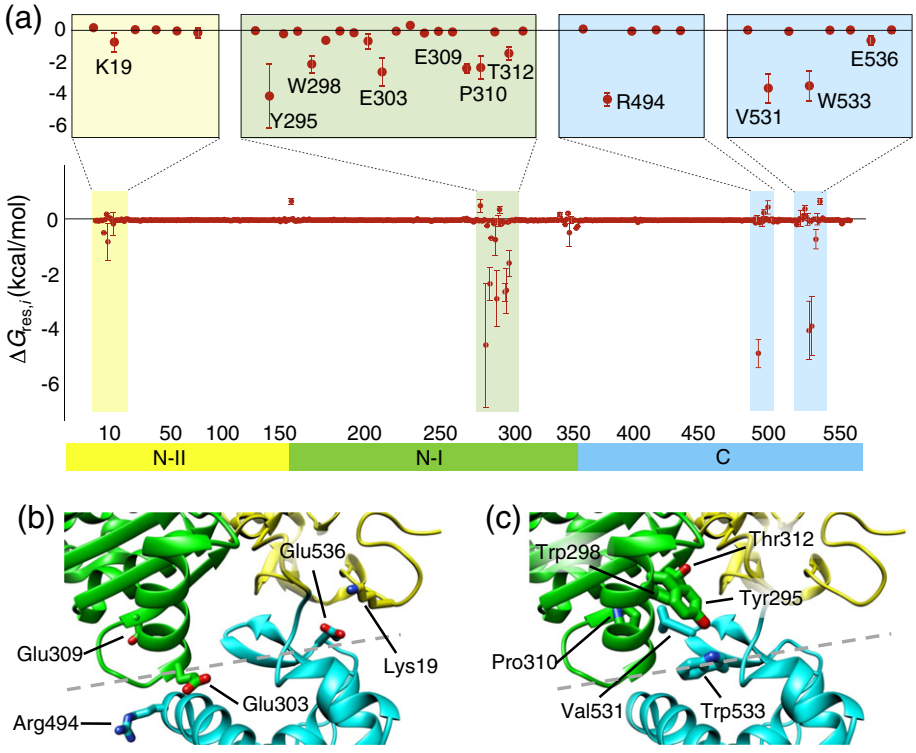

Fig. 2. Individual residue contributions to ΔG_{EC} allow for the elucidation of energetically important residues. (a) Per-residue decomposition $\Delta G_{res,i}$ of the overall free energy change of gp17 compaction. Most residues are not involved in compaction and thus have a free energy change close to zero. Residues that contribute appreciably are all located at the interface between the N- and C-terminal domains and can be grouped into four main clusters. The slightly favorable contributions of residues in the hinge region close to position 350 are an artifact of the MM-GBSA-based approach that requires the N- and C-terminal domains to be defined as separated molecules. The insets on the top show expanded views of the data corresponding to the four clusters, highlighting 11 residues exhibiting $\Delta G_{res,i}$ less than −0.5 kcal/mol. Location of the five charged residues (b) and six uncharged residues (c) identified as energetically important above shows proximity to the inter-domain interface, indicated by the gray broken line.

compaction. Since the compaction mechanism studied here relies on a conformational change involving the formation of an interface between two domains, much of the free energy is expected to arise from residues at or close to this interface. Indeed, we find that −31.9 ± 3.2 kcal/mol, or 90%, of the total change in free energy arises from the 46 residues residing at the interface (defined as those with at least one atom within 5 Å of the other domain). Summing up the contributions from charged and uncharged residues at the interface reveals that charged residues contribute −12.0 ± 1.5 kcal/mol (~37%) of this free energy while uncharged residues contribute −20.0 ± 2.9 kcal/mol (~63%). Dissecting these free energies further into polar and nonpolar contributions reveals that significant portions of the free energy contributions from charged and uncharged residues indeed arise from polar and nonpolar interactions, respectively. These results revealing a larger free energy contribution from uncharged residues as compared to charged residues thus expand upon the original model for force generation proposed by Sun *et al.* [25], which implicated electrostatic interactions from charged residues as the main driver of the compaction transition.

We also find that a further subset of 11 residues contributes >80% of the overall free energy change, each contributing less than −0.5 kcal/mol to ΔG_{EC}, as listed in Table 2. The structural context of each of these residues is shown in Fig. 2b and c. Of these 11 energetically important residues, five are charged: Lys19, Glu303, Glu309, Arg494, and Glu536, all of which were proposed to play a role in compaction based on the crystal structure. However, we find that seven of the twelve charged residues (Lys23, Lys305, Lys493, Lys504, Asp505, Glu528, and Glu537) originally proposed to be potentially involved do not contribute a favorable free energy change and are therefore unlikely to be directly involved in force generation. In addition, we find that six uncharged residues contribute very favorable free energy changes: Tyr295, Trp298, Pro310, Thr312, Val531, and Trp533.

Table 2. Per-residue free energy contributions made by the most energetically important residues and further breakdown of these contributions into polar and nonpolar components

Residue[a]	Polar[b]	Nonpolar[b]	Total[b]
$Lys19^{(+, N)}$	−2.91 (4.47)	2.17 (0.41)	−0.73 (0.67)
$Tyr295^{(0, N)}$	−0.84 (0.64)	−3.40 (2.12)	−4.24 (2.14)
$Trp298^{(0, N)}$	−0.80 (0.56)	−1.35 (0.58)	−2.16 (0.60)
$Glu303^{(-, N)}$	0.02 (1.68)	−2.69 (0.93)	−2.67 (0.97)
$Glu309^{(-, N)}$	−2.54 (3.24)	0.11 (0.18)	−2.44 (0.34)
$Pro310^{(0, N)}$	0.14 (0.29)	−2.52 (0.78)	−2.38 (0.79)
$Thr312^{(0, N)}$	−0.82 (0.52)	−0.63 (0.42)	−1.46 (0.46)
$Arg494^{(+, C)}$	−3.22 (2.71)	−1.29 (0.25)	−4.52 (0.51)
$Val531^{(0, C)}$	0.17 (0.38)	−3.91 (1.02)	−3.75 (1.02)
$Trp533^{(0, C)}$	−0.75 (0.27)	−2.84 (0.98)	−3.60 (1.02)
$Glu536^{(-, C)}$	−1.70 (4.05)	1.05 (0.21)	−0.65 (0.35)

[a] Symbols +, −, and 0 within parenthesis denote positively charged, negatively charged, and uncharged residues, while N and C denote residues in the N- and C-terminal domains, respectively.

[b] Numbers within parentheses represent standard errors in the reported values. A description of how these errors were estimated is provided in Materials and Methods.

Recently, we measured the DNA packaging activity by single-molecule assays in terms of three metrics: average packaging rate, motor velocity (rate not including pauses and slips), and percent time packaging for T4 motors containing wild type or mutant gp17s (Glu537Lys, Glu303Lys, and Glu537Lys-Lys305Asp) in which one or two charged interface residues proposed to be important for compaction were replaced by oppositely charged residues [27]. We observed that all three mutants exhibited impairments in motor activity relative to wild-type gp17. To investigate whether the per-residue free energy contributions calculated here can explain the experimentally observed variations in packaging, we examined the correlation between $\Delta G_{res,i}$ computed for the mutated residues and the three experimental metrics of motor activity. As explained in Ref. [29], we performed this correlation analysis for measurements under a large applied load force (50 pN), where the motor's force-generating capability is strongly challenged. As shown in Fig. 3a–c, we find a strong correlation between per-residue free energy change and each experimental metric of motor activity, indicating that the residues contributing the most free energy to compaction indeed cause the greatest impairment to motor activity when mutated. That the predicted importance of individual residues gained from free energy decomposition relates well to experimental findings suggests that our MD simulation-based free energy calculations provide a reasonable approximation of the energetics governing the compaction transition.

Charge/charge interactions at the interface and their role in gp17 compaction

We next examined in more detail the electrostatic interactions between each pair of oppositely charged residues at the domain interface, in part to investigate why only a subset of all possible charged residues contributed favorably to ΔG_{EC}. Due to screening and solvation effects, the interactions between oppositely charged residues in proteins are highly distance dependent [31]. For instance, “salt bridges”, defined as ion pairs where the distance between each pair of oppositely charged ion on the interacting residues is <4 Å, are almost always favorable because the electrostatic attraction more than compensates the loss in solvation of ions due to pairing. On the other hand, “long-range ion pairs” in which each ion pair distance is >4 Å are almost always unfavorable [32]. Thus, we examined

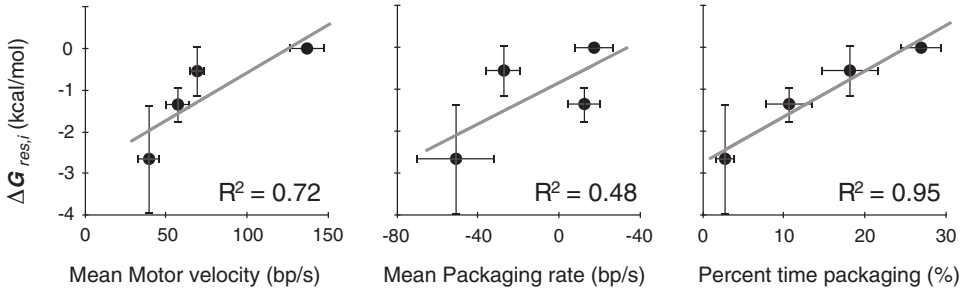

Fig. 3. Correlations between experimental metrics of motor activity and residue-level free energies. Symbols represent free energy contributions $\Delta G_{res,i}$ of residues that were altered by mutation in experiments *versus* the indicated metric of packaging activity measured for motors assembled with the altered residues. Data also include the activity of the wild-type motor that is assigned $\Delta G_{res,i} = 0$. The packaging rate includes pauses and slips that are not included in the motor velocity [23]. Lines show linear regressions and corresponding Pearson correlation coefficients (min = 0, max = 1) are indicated.

changes in distances between ion pairs (Fig. 4) and in solvent occupancy near charged groups (Fig. 5). We also dissected the per-residue free energy contribution of each charged residue into polar and nonpolar components (Table 2).

Analysis of ion pair distances between all 12 charged residues near the domain interface (Fig. 4) revealed three main types of electrostatic interactions: strong salt bridges across the interface that form only in the compact state of gp17 (Glu309–Arg494 and Lys19–Glu536), long-range ion pairs across the interface that remain largely unchanged upon compaction (Lys23–Glu537), and strong intra-domain salt bridges that also remain unchanged upon compaction (Glu303–Lys305, Lys504–Glu508, and Asp505–Lys509). The other pairs of charged residues were found to be too distant to form any ion pairs (Fig. 2c).

We find that, among all ion pairs, the most energetically favorable one is between Glu309 and Arg494 that contributes -6.92 ± 0.60 kcal/mol to ΔG_{EC} (Table 2), which is ~20% of the total free energy of compaction. The reason is two fold. First, the interaction distance between the corresponding ions is only 3.50 ± 0.97 Å in the compact state, much shorter than that in the extended state (8.30 ± 1.87 Å) (Fig. 4d), leading to favorable electrostatic attraction between the two residues (Table 2). Second, both residues are located on a partially solvent-exposed face of the protein. Therefore, we expect the desolvation penalty to be partly mitigated as a salt bridge forms between the two residues. In fact, Arg494, which is not even solvated in the extended state, is able to share the solvation of Glu309 by forming a close association with it in the compact state, leading to favorable solvation energy (Table 2). This effect is clearly seen in the solvent occupancy maps of the two residues in the two states (Fig. 5c and d). Based on this free energy change, we propose that the interaction between Glu309 and Arg494 plays a dominant role in the compaction of gp17, a finding that is consistent with experimental studies showing complete abrogation of packaging activity when Glu309 is changed to a lysine [29].

Residues Lys19 and Lys23 appear to be capable of forming interactions with either Glu536 or Glu537 in the X-ray crystal structure (Fig. 2b). However, we find that ion pairs are formed exclusively between Lys19 and Glu536 and between Lys23 and Glu537. While the interaction between Lys19 and Glu536 becomes stronger with compaction, reducing by ~2 Å from 4.77 ± 0.57 Å in the extended state to 2.80 ± 0.28 Å in the compact state (Fig. 4a), the interaction between Lys23 and Glu537 decreases by ~1 Å, from 5.84 ± 2.57 Å to 4.77 ± 0.99 Å (Fig. 4b). The favorable interaction between Lys19 and Glu536 is partly offset by complete desolvation of the ionic groups on the two residues (Fig. 5a and e) and the resulting salt bridge contributes only -1.38 ± 0.76 kcal/mol (Table 2).

The gp17 crystal structure shows a cluster of charged residues at the center of the domain interface and suggests that Glu303 and Lys305 residues on the N-terminal domain might form ion pairs with Lys504 and Asp505 residues on the C-terminal domain (Fig. 2b). However, upon inspection of the configurations sampled during MD simulations and ion pair distances, we find that neither of these interactions is formed. Instead, Glu303 and Lys305 interact very closely (3.52 ± 0.59 Å) with each other to form a strong intra-domain salt bridge that stabilizes an important loop connecting elements that contain energetically important residues Glu309, Tyr295, and Trp298 (Fig. 4c). Interestingly, the favorable per-residue contribution of Glu303 does not arise from its electrostatic interactions, which remain constant during compaction, but rather, it arises from the strong nonpolar contacts that Glu303 makes with residues across the domain in the compact state (Table 2), possibly facilitated by the removal of a water molecule from the vicinity of this residue upon compaction (Fig. 5b). Similarly, Lys504 and Asp505 are also involved in

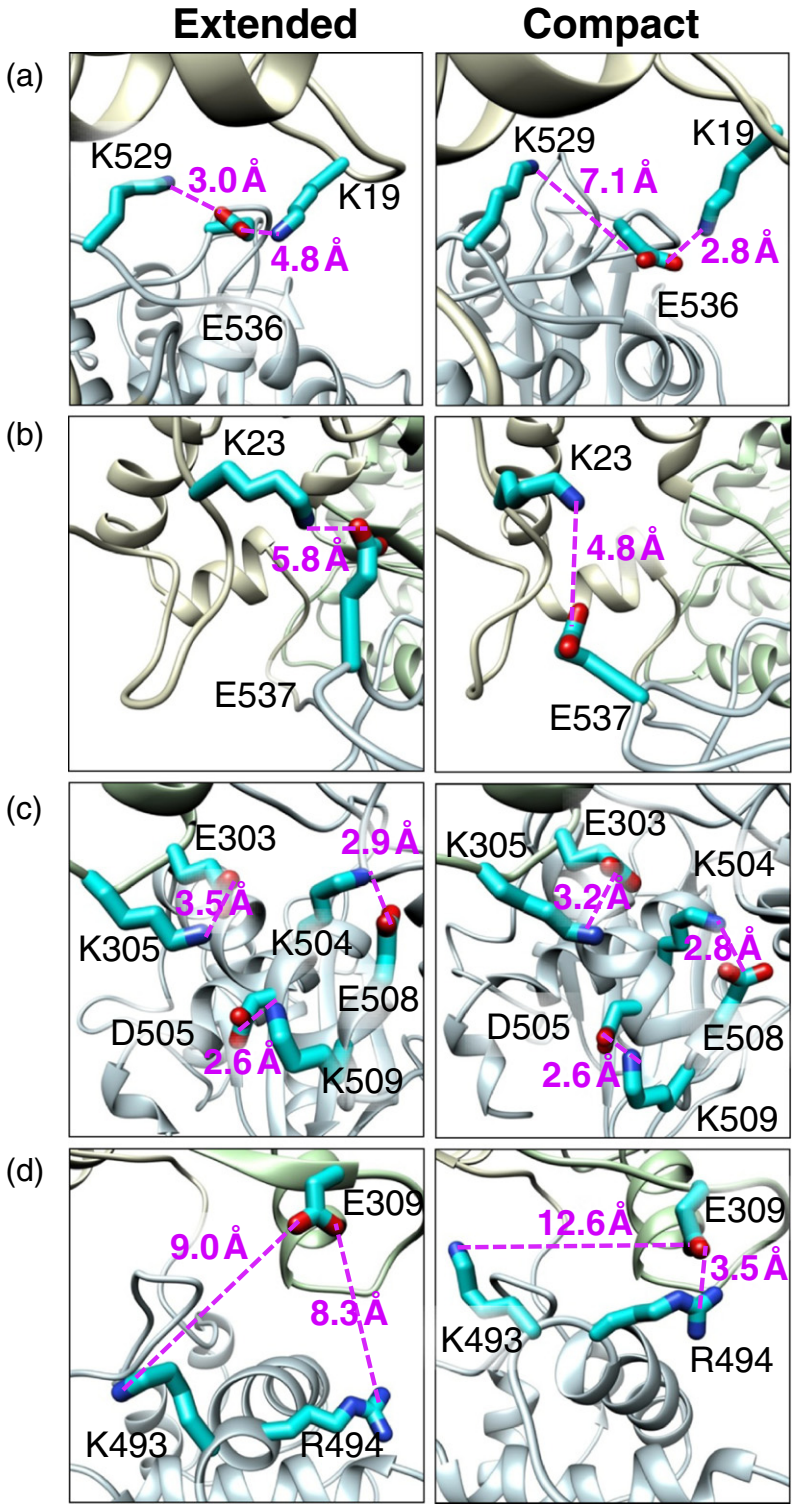

Fig. 4. Changes in charge/charge interactions upon gp17 compaction. Representative conformations of the gp17 domain interface in the compact (left panel) and extended states (right panel) highlighting differences in ion-pairing interactions between the two states. The pink broken lines denote the interaction between charged atoms on two oppositely charged residues (shown in cyan and labeled) and the corresponding distances averaged over the MD simulations are labeled. The four panels focus on different ion-pairing interactions, showing that Lys19–Glu536 (a) and Glu309–Arg494 (d) ion pairs are important for compaction due to a large decrease in their distances during compaction. The panels also show that Lys23–Glu537 interaction is not important for compaction as the two residues remain distant even in the compact state (b) and that several other charged residues are also not important for compaction due to their preference to form ion pairs within their own domain rather than across domains (c).

forming salt bridges with other charged residues in the C-terminal domain, Glu508 and Lys509, in both the extended and compact forms of gp17 (Fig. 4d). Moreover, both these salt bridges seem to be involved in "capping" the same α-helix, a common function of salt bridges in proteins [33].

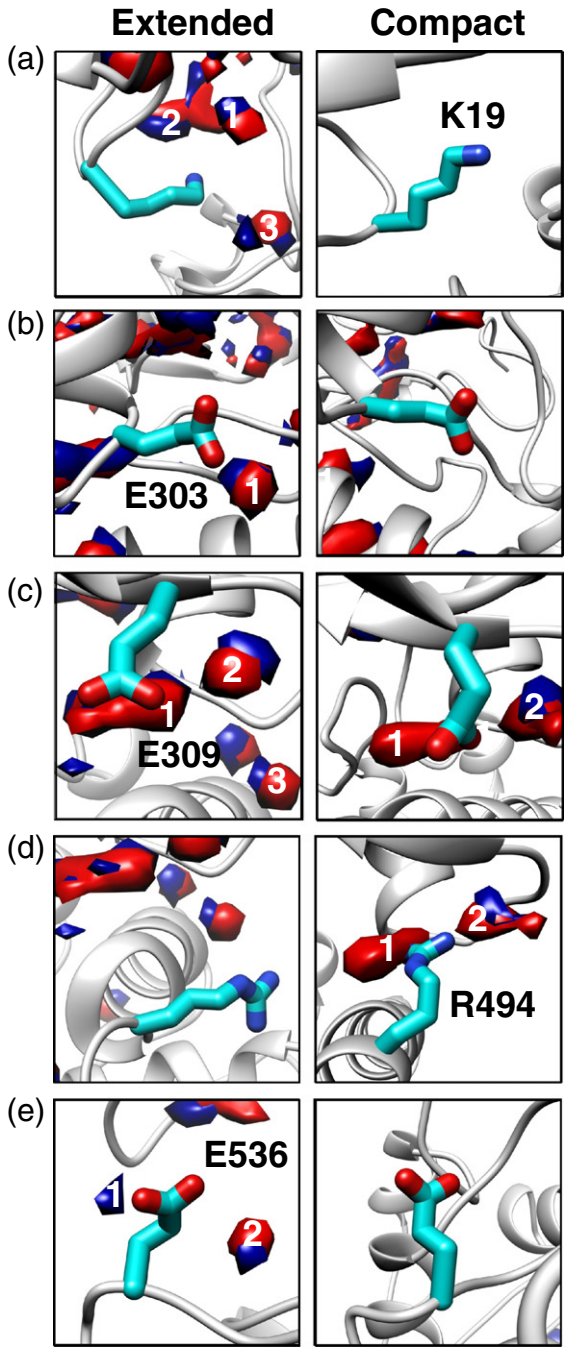

Fig. 5. Changes in solvation of charged residues at the interface upon compaction. Calculated map of water occupancy surrounding important charged amino acids (cyan) at the domain interface in gp17. Contour surfaces are labeled dark blue for hydrogen and red for oxygens and numbered when they are sufficiently proximal to the charged residue. (a–e) The surrounding solvation of Lys19, Glu303, Glu309, Arg494, and Glu536 in the extended (left panel) and compact (right panel) states.

Taken together, the five interfacial charged residues that yielded favorable per-residue free energies do so due to formation of strong salt bridges (Lys19–Glu536 and Glu309–Arg494) and vdW contacts (Glu303) across the interface upon compaction. In contrast, the seven interface residues that contributed negligible or unfavorable free energies do so due to their inability to form any salt bridges (Lys493, Glu528) or due to their involvement in intra-domain salt bridges (Lys305, Lys504, Asp505) or weak long-range ion pairs (Lys23, Glu537).

Nonpolar contacts at the interface and their role in compaction

While charged residues mediate few strong interactions with each other, hydrophobic residues form many parallel weak vdW interactions with their neighbors. Our free energy decomposition identified the involvement of six uncharged residues in gp17 compaction (Table 2), five of which are nonpolar residues (Tyr295, Trp298, Pro310, Val531, and Trp533) and one of which is a polar residue (Thr312). Collectively, these six residues were found to contribute 46% of the total free energy of compaction. To investigate how these uncharged residues were involved in stabilizing the compact state, relative to the extended state, we mapped compaction-induced changes in vdW interactions mediated by these residues (Fig. 6) and their solvation (Fig. 7), both indicators of the formation of a stable, solvent-excluding interface.

We found that Tyr295 occupies a position that occludes several other hydrophobic residues from solvent interactions (Fig. 6b). Upon compaction, a rotation of this residue's aromatic ring reduces its exposure to the solvent, allowing it to form hydrogen bonds with a water molecule through its hydroxyl group (Fig. 7a). In the compact state, Tyr295, due to its large size, forms 922 vdW contacts, on average, with 15 other residues, an increase of over 79 contacts from the extended state. Both these favorable effects cause Tyr295 to have the largest per-residue free energy contribution to compaction (-4.23 ± 2.14 kcal/mol; Table 2) of all uncharged residues present at the interface.

Unlike Tyr295, Trp298 is buried deeply within the interface region (Fig. 2b). It is located in the center of the α-helix connecting the ATP binding pocket to the interface. Trp298 contributes a free energy change of -2.16 ± 0.60 kcal/mol upon compaction, with nonpolar and electrostatic interactions contributing -1.35 ± 0.58 kcal/mol and -0.81 ± 0.56 kcal/mol, respectively. The favorable nonpolar contribution arises from Trp298's 1179 vdW contacts, on average, in the compact state, an increase of 64 contacts from the extended state (Fig. 6b), while the favorable electrostatic contribution arises from the formation of a channel at the interface in the compact state that allows for the indole nitrogen of Trp298 to hydrogen bond with a water molecule (Fig. 7b).

Pro310 exhibits a similar orientation in both the compact and extended states (Fig. 7c) and is likely

(a)

Residue	vdW contacts$_E$	vdW contacts$_C$	Δ vdW contacts$_{EC}$
Tyr 295	843.0 (8.3)	922.0 (5.9)	79.1 (10.2)
Trp 298	1115.2 (8.3)	1179.3 (11.3)	64.1 (14.0)
Pro 310	636.2 (8.4)	696.0 (6.6)	59.7 (10.7)
Thr 312	543.7 (5.2)	555.1 (8.4)	11.4 (9.8)
Val 531	579.5 (9.7)	579.3 (8.6)	-0.2 (12.9)
Trp 533	1175.0 (9.2)	1196.3 (10.9)	21.3 (14.3)

(b)

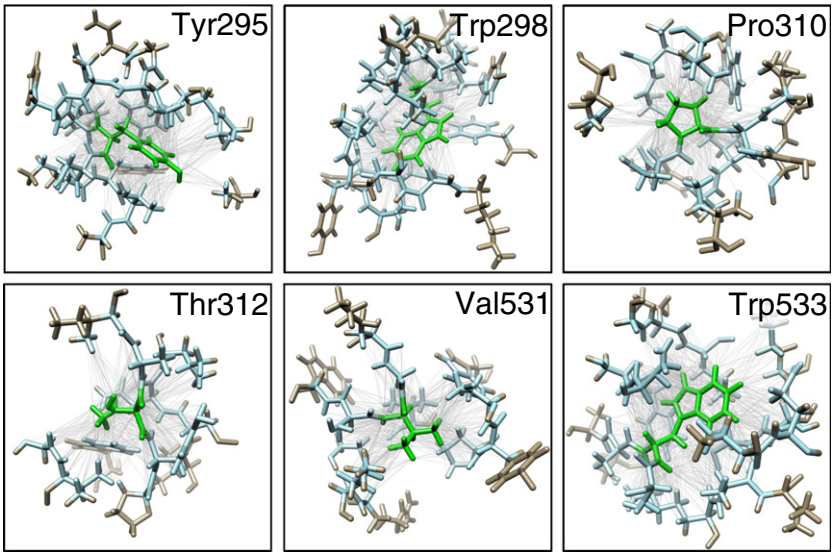

Fig. 6. Water-excluding vdW interactions formed by the six energetically important uncharged amino acids with surrounding residues. (a) The average number of solvent-excluding interactions formed by each residue in the extended and compact conformations of gp17 and the change upon compaction. Standard error within parentheses. (b) Molecular details of the large number of interactions formed by each of these six residues shown in green, in the compact conformation. Each individual solvent-excluding vdW interaction is shown as a gray line, while contacting atoms are shown in light blue.

involved in the stabilization of a β-turn [34]. Pro310 contributes a free energy change of −2.38 ± 0.79 kcal/mol toward compaction, all of which is derived from nonpolar interactions due to an increase in the vdW contacts. It forms 59 more vdW contacts in the compact state (for a total of 696) relative to the extended state (Fig. 6a).

In general, threonines are not involved in the formation of interfaces between proteins due to their polarity. However, Thr312 plays a large role in the energetics of gp17 compaction by occluding the central hydrophobic patch from solvation, similar to Tyr295. Interestingly, Thr312 displays a similar number of vdW contacts in the compact state (555), relative to the extended state (543) (Fig. 6a). This may seem contradictory, but the minimal increase in contacts allows for Thr312 to retain its ability to form hydrogen bonds with water, similar to its conformation in the extended state (Fig. 7d).

Val531 occupies a position at the center of the hydrophobic patch in the interface. The compaction transition leads to a ~90° rotation of the side chain with respect to the backbone, resulting in a large reduction in the surface area exposed to solvent (Fig. 7e) and the same number of vdW contacts with neighboring residues in the compact state (579) and the extended state (579) (Fig. 6a). This leads to a large free energy contribution of −3.74 ± 1.02 kcal/mol, most of which is contributed by nonpolar interactions (Table 2).

Finally, Trp533 plays a strong role in compaction by effecting a large degree of desolvation needed to form a stable interface due to its large size. Upon compaction, the water molecule nearest to Trp533 is pushed away by 3 Å (Fig. 7f), a significant change that leads Trp533 to form 21 additional vdW contacts, on average, in the compact state (1196 contacts, relative to 1175 contacts in the extended state; Fig. 6a), explaining its favorable free energy contribution of −3.59 ± 1.02 kcal/mol (Table 2).

We also note that, in most cases, the change in number of vdW contacts mediated by a residue upon compaction correlates very well with the corresponding free energy change contributed by that residue.

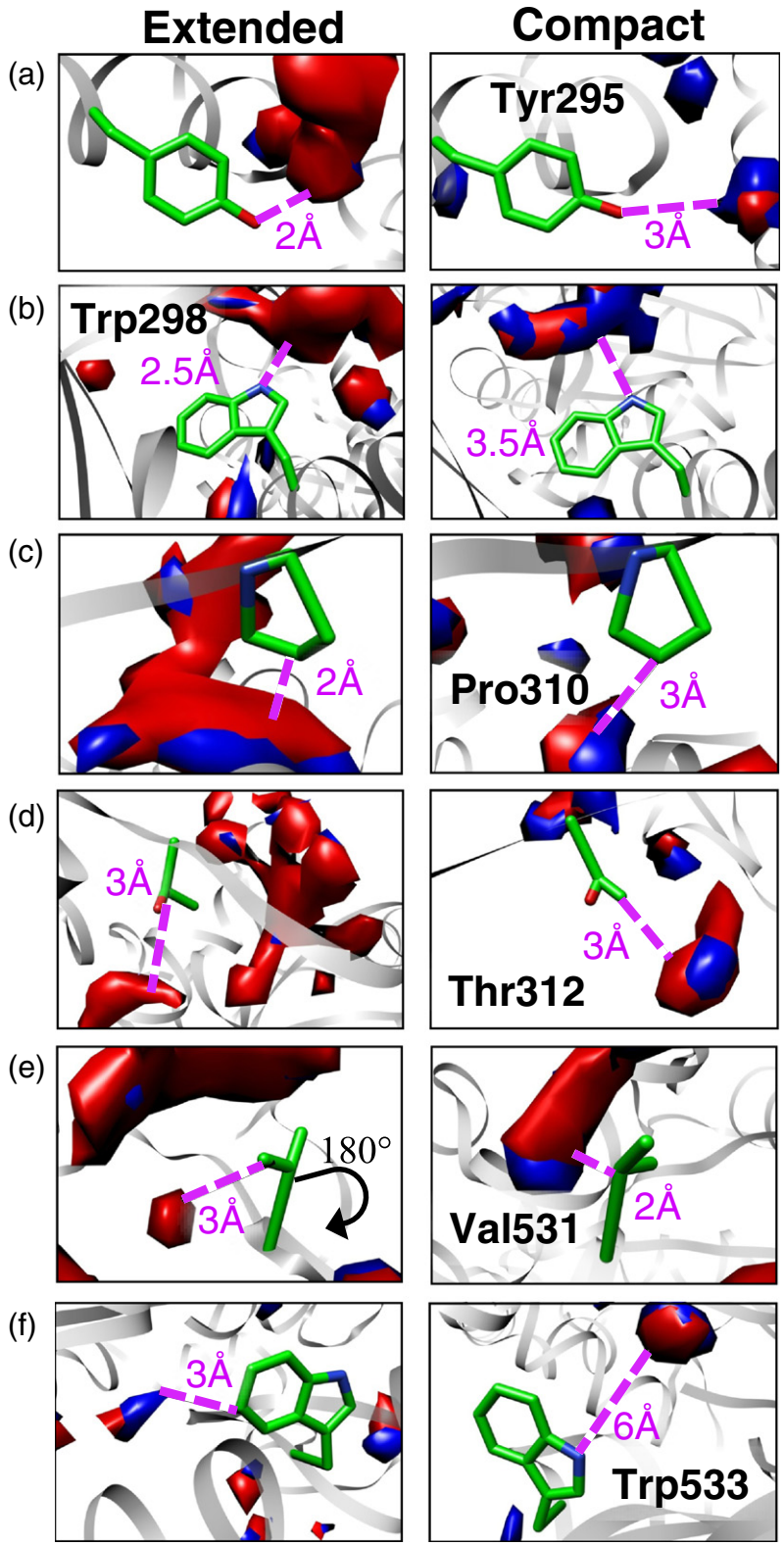

Fig. 7. Distance to closest water molecule from six energetically important uncharged residues. Calculated distances between uncharged residues (green) and the nearest water molecule (dark red/blue), as described in Materials and Methods. Shown here are the uncharged amino acids contributing the most to the free energy of gp17 compaction: Tyr295 (a), Trp298 (b), Pro310 (c), Thr312 (d), Val531 (e), and Trp533 (f).

This shows that the main role of these uncharged residues within the interface is to exclude water to allow for close association of the faces of the two domains. Val531 is the only residue that does not follow this trend because the free energy change at this position is due solely to favorable rotation of a

side chain that forces water molecules out of the interface.

Discussion

We have elucidated the specific molecular interactions involved in driving a reported compaction transition in bacteriophage T4 DNA packaging motor, gp17. Recently, Sun *et al.* proposed that this conformational transition is responsible for generating the "power stroke" that translocates DNA into the viral capsid against large resistive forces and that the transition is mediated by electrostatic interactions between complementarily charged pairs of residues on the N- and C-terminal domains [25]. Using a combination of MD simulations, free energy decomposition, and structural analyses, we have shown here that the proposed conformational transition is highly energetically favorable. We also show that the transition is not governed solely by electrostatic interactions between charged pairs of residues alone but that interactions mediated by uncharged residues play an equal if not greater role. Our calculations reveal the existence of 11 critical residues at the domain interface that contribute $>80\%$ of the favorable free energy associated with the compaction transition, of which 5 residues are charged, 5 are hydrophobic, and 1 is polar. We have dissected the role played by each residue in promoting the compaction transition in terms of changes in the salt bridges, vdW contacts, and hydrogen-bonding interactions with water mediated by each residue as gp17 undergoes the transition.

Our results not only help to identify the underlying interactions leading to DNA translocation but also serve to expand the possibilities for further testing of this proposed mechanism of DNA translocation via targeted mutagenesis. The previous hypothesis that charged residues mediate force generation has now been refined—we have shown that fewer than half of the 12 charged residues at the inter-domain interface function directly in force generation by forming key salt bridges. There is excellent correlation between the per-residue free energy change and available experimental data on the effects of site-directed mutations of charged residues. Alterations of the six uncharged residues we have identified are also expected to cause significant impairments in motor function. In fact, mutation of one of these identified hydrophobic residues (Trp533Ala) has already been shown through a bulk assay to impair DNA packaging [25]. Additionally, the interaction between Lys19 and Glu536 is lengthened in the extended state, partially due to the proximity of a competing interaction with Lys529. If the interaction between Lys19 and Glu536 is important to initiating compaction, then mutation of Lys529 might cause difficulties in attaining the extended state, resulting in potential reduction in the velocity or force generation capabilities of the motor. Finally, because we have been able to discern between competing charge pairs such as Lys493–Glu309 and Arg494–Glu309, it is conceivable that motor activity could even be enhanced by removing the nonsalt bridging residue to strengthen the dominant ion pair, in this case, the salt bridge between Arg494 and Glu309.

While our computational results are in generally good agreement with available experiments, one must still consider these results in proper perspective due to the approximate nature of these calculations. First of all, the semi-empirical force fields used in all MD simulations including ours are simplified approximations of the true electronic interactions between atoms. Second, while we have attempted to perform our MD simulations as exhaustively as possible with the available computational resources, the simulations might still not be able to fully sample all relevant conformational states, leading to inaccuracies in the computed ensemble averages. Third, the MM-GBSA approach uses a mean-field approximation to drastically speed up the calculation of solvation free energies. Fourth, changes in the configurational entropy of gp17 as it undergoes the compaction transition have been neglected due to the enormous computational requirements of such a calculation. Lastly, as mentioned earlier, due to our limited knowledge on the structure of the pentameric motor complex, we are currently restricted to examining the compaction transition in monomeric forms of gp17. Nevertheless, we believe that our calculations capture well the leading-order contributions of residues and interactions involved in the compaction transition in gp17, especially given the strong correlation with the experimental trend of impairments.

In conclusion, our study refines the original model proposed by Sun *et al.* for force generation in gp17, as summarized schematically in Fig. 8. Our calculations indicate that only a few charged residues contribute significantly to compaction and that a number of uncharged residues also play a significant role. In particular, the compaction step is most stabilized by the formation of a very favorable salt bridge between residues Arg494 and Glu309. Once the interface is nearly closed, other inter-domain salt bridges and vdW interactions between adjacent hydrophobic residues conclude the power stroke and stabilize the interface by forming solvent-excluding interaction networks that aid in the desolvation of the interface. The conformational change bringing the N- and C-terminal domains together in gp17 to drive DNA translocation is analogous in some ways to the large rearrangement used to reset the myosin motor [35] and to the F_o ATP synthase subunit coordination that is carried out by a single arginine residue orienting the surrounding amino acids for proton transfer [36]. In both systems, a conformational change is initiated by longer-range ion pairing and is continued by vdW or polar interactions. Future studies should reveal differences and similarities between viral DNA packaging motors

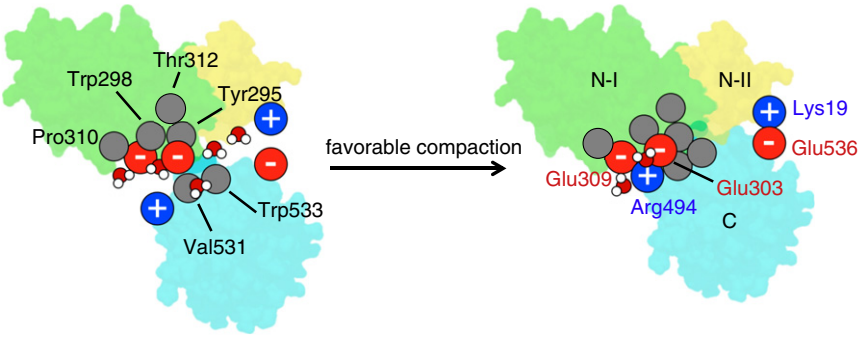

Fig. 8. Refined model for interactions governing gp17 compaction. As illustrated schematically, only a few charged residues contribute significantly to compaction, and a number of uncharged amino acids, along with solvation effects, also play a significant role. Red spheres indicate negatively charged residues, blue indicates positively charged residues, gray indicates uncharged residues, and red-white spheres indicate water molecules.

such as gp17 and other types of molecular motors found in nature.

Materials and Methods

Preparation of initial configurations

The MM-GBSA approach [30] requires carrying out exhaustive all-atom MD simulations of the compact and extended states of gp17 in explicit solvent and ions, starting from reasonable initial configurations of the two states. To obtain these initial configurations, we immersed the gp17 crystal structure in the compact state (PDB code 3CPE) in a TIP3P water box with a minimum padding of 10 Å by using the *Solvate* function in VMD [37]. We used the *Autoionize* function in VMD to neutralize the system and add 150 mM NaCl. The resulting system was energy minimized with 100 steps of steepest descent and then equilibrated with 0.5-ns-long MD simulations to yield the initial configuration of the compact form of gp17. To obtain the initial configuration of the extended state, we carried out additional steered MD simulations of the compact configuration prepared above. In these simulations, the C-terminal domain was slowly pulled away from the N-terminal domain along the vector connecting the centers of mass of the two domains at a velocity of 0.0002 Å/fs until the two domains were separated by a further 7 Å relative to the starting structure. The resulting extended structure was further equilibrated using 0.5-ns-long MD simulations to yield the initial configuration of the extended form of gp17.

The energy minimizations and MD simulations described above were carried out in NAMD [38] using the CHARMM 27 force field [39]. All MD simulations were performed with periodic boundary conditions at a constant temperature of 300 K and a constant pressure of 1 atm. A SHAKE algorithm was used to keep all bonds involving hydrogen atoms rigid. A cutoff distance of 12 Å was used for computing short-range nonbonded interactions and a particle mesh Ewald method with grid spacing of 1 Å was used for computing electrostatic interactions. The temperature was maintained constant using a Langevin thermostat with a damping constant of 1 ps and the pressure was maintained constant using a Langevin piston with a period of 100 fs and a damping time constant of 50 fs. A time step of 2 fs was employed for integrating the equations of motion.

In addition to the compact and extended initial configurations prepared above, we generated three more sets of initial configurations. This allowed us to perform four independent MM-GBSA calculations, each starting from a different set of initial configurations, to improve our free energy estimates. To this end, we performed 50-ps-long MD simulations on the original set of initial configurations at four different temperatures of 300 K, 310 K, 320 K, and 330 K. A weak restraint was imposed on all heavy atoms through a harmonic potential with a spring constant of 2.0 kcal/mol/Å^2. This procedure allowed the configurations to depart significantly from the starting configuration while remaining stable at the nonphysiological temperatures. We carried out additional 1 ns of MD simulations during which the restraints were removed and the temperatures were brought back to 300 K.

Free energy calculations and decomposition

While the free energy change ΔG_{EC} of the compaction transition in gp17 can in principle be calculated from all-atom MD simulations using exact formalisms such as umbrella sampling and free energy perturbation, these methods prove to be computationally intractable for systems as large as gp17. Consequently, we used the more efficient method of MM-GBSA [30], which permits quick estimates of ΔG_{EC} from all-atom MD simulations by approximating the solvation free energy using the generalized Born model; this approach also conveniently provides interaction- and residue-level contributions to the overall free energy change [40].

However, MM-GBSA is designed to calculate intermolecular binding free energies, that is, free energy difference between bound and completely unbound states of two separate molecules, whereas ΔG_{EC} is the free energy difference between two differently bound states (extended and compact) of the same molecule (gp17). We therefore adapt our application of the MM-GBSA approach to computing ΔG_{EC} by (1) treating the N- and C-terminal domains of gp17 as two separate molecules divided at the flexible hinge connecting the two domains and by (2) computing the "binding" free energies $\Delta G_{bind,C}$ and $\Delta G_{bind,E}$

associated with assembling the compact and extended states from a common isolated state in which the two domains are too far to interact, calculations that are directly amenable to MM-GBSA. This indirect approach then allows us to obtain the free energy of compaction ΔG_{EC} via $\Delta G_{EC} = \Delta G_{bind,C} - \Delta G_{bind,E}$.

The binding free energies $\Delta G_{bind,E}$ and $\Delta G_{bind,C}$ were computed from snapshots of the extended- and compact-state configurations of gp17 by using the *mm_pbsa.pl* script in AMBER 10 [41]. We used a total of 6400 snapshots for each state, gathered from four 8-ns-long explicit solvent MD simulations and spaced 5 ps apart. The simulations were started from the initial configurations of the extended and compact states generated above and were carried out using NAMD software with CHARMM 27 force field at 300 K temperature, 1 atm pressure, and 150 mM NaCl using the same simulation protocol we described earlier for equilibrating the initial configurations. In these calculations, the N-terminal domain (residues 1–359) and the C-terminal domain (residues 360–560) were treated as two separate molecules, called receptor and ligand, respectively. The binding free energy $\Delta G_{bind,i}$ (i = C, E) was then computed as

$$\Delta G_{bind,i} = \Delta E_{MM,i} + \Delta G_{solv,i} - T\Delta S_{conf,i}, \quad (1)$$

where $\Delta E_{MM,i}$, $\Delta G_{sol,i}$, and $T\Delta S_{conf,i}$ represent contributions from changes in the molecular mechanics energy, solvation free energy, and entropy to the overall free energy change.

The molecular mechanics contribution $\Delta E_{MM,i}$ was computed as the total interaction energy between the two gp17 domains in the complex state, given by the sum of vdW $\Delta E_{vdW,i}$ and electrostatic (Coulombic) and $\Delta E_{ele,i}$ interaction energies [41]. The solvation contribution $\Delta G_{sol,i}$ was calculated via continuum, mean-field description of solvent, as the sum of polar and nonpolar components. The polar component $\Delta G_{pol,i}$ due to solvent dielectric and salt screening effects was computed using the generalized Born approach [42]. For this calculation, the solute and solvent dielectric constants were set to 1 and 80, respectively. The nonpolar component $\Delta G_{np,i}$ due to water/solute vdW interactions and cavity formation was calculated as the change in the solvent-accessible surface area upon complex formation multiplied by the surface tension. We used a water probe of radius 1.4 Å for calculating solvent-accessible surface area and used a surface tension of 0.0072 kcal/mol/Å^2. The entropic contribution $T\Delta S_{conf}$, typically computed using normal mode analysis [43], was not calculated, as these calculations converge very slowly. Moreover, our focus is on computing residue- and interactions-level contributions to the compaction free energy, and the normal mode entropy is a collective property that cannot be dissected to the level of individual molecular interactions or residues.

The abovementioned calculations yielded various components of the compact- and extended-state binding free energies that were then used to obtain interaction-level contributions—vdW, Coulombic, polar solvation, and nonpolar solvation—to the free energy of compaction ΔG_{EC}:

$$\Delta E_{vdW,EC} = \Delta E_{vdW,C} - \Delta E_{vdW,E}, \quad (2)$$

$$\Delta E_{ele,EC} = \Delta E_{ele,C} - \Delta E_{ele,E}, \quad (3)$$

$$\Delta G_{pol,EC} = \Delta G_{pol,C} - \Delta G_{pol,E}, \quad (4)$$

$$\Delta G_{np,EC} = \Delta G_{np,C} - \Delta G_{np,E}. \quad (5)$$

These contributions were also used to obtain the total polar (Coulombic + polar solvation) and total nonpolar (vdW + nonpolar solvation) contributions to ΔG_{EC} via:

$$\Delta G_{tot\text{-}pol,EC} = \Delta E_{ele,EC} + \Delta G_{pol,EC}, \quad (6)$$

$$\Delta G_{tot\text{-}np,EC} = \Delta E_{vdW,EC} + \Delta G_{np,EC}. \quad (7)$$

Because polar uncharged and hydrophobic residues also hold partial charges in the force field, the total polar contribution $\Delta G_{tot\text{-}pol,EC}$ includes Coulombic interactions between all residues, not just the charged ones that are expected to contribute the most. Similarly, all residues exhibit vdW interactions, and therefore, the total nonpolar contribution $\Delta G_{tot\text{-}np,EC}$ includes vdW interactions from all types of residues, though hydrophobic residues are expected to contribute more. Also, since the total polar contribution accounts for the mitigation of Coulombic interactions due to salt screening and solvation via the $\Delta G_{pol,EC}$ term, $\Delta G_{tot\text{-}pol,EC}$ is a truer indicator of the contribution of electrostatic interactions than $\Delta E_{ele,EC}$.

To obtain the contributions to ΔG_{EC} from each residue, denoted by $\Delta G_{res,i}$ for residue i, we used the free energy decomposition function in MM-GBSA (by setting DCTYPE = 2 to indicate per-residue decomposition) in AMBER 10. Details on how the free energies contributions from vdW, electrostatic, and polar/nonpolar solvation are divided on a per-residue basis have been described elsewhere [44].

Estimating statistical errors in the computed free energies

The MM-GBSA algorithm we use outputs the average binding free energy ΔG_{bind} and its four components ΔE_{ele}, ΔE_{vdW}, ΔG_{np}, and ΔG_{pol} from a single MD trajectory of a molecular complex. We calculated the errors in $\Delta G_{bind,i}$, $\Delta E_{ele,i}$, $\Delta E_{vdW,i}$, $\Delta G_{np,i}$, and $\Delta G_{pol,i}$ as SEM (*s*tandard *e*rror of the *m*ean) obtained from application of this protocol to the four separate 5-ns-long MD trajectories obtained for each gp17 state (i = C, E). We used standard error propagation formulas to obtain errors in the quantities we report involving sums or differences in the abovementioned five outputs, for example, the error in ΔG_{EC} ($\Delta G_{bind,C} - \Delta G_{bind,E}$) was obtained from the SEMs of $\Delta G_{bind,C}$ and $\Delta G_{bind,E}$. The MM-GBSA free energy decomposition algorithm outputs the average free energy contribution from each residue and its four components (vdW, electrostatic, polar solvation, and nonpolar solvation) from an MD trajectory. Applying this protocol to the four MD trajectories of each state then yielded for each state the means and SEMs of the per-residue contribution and for each of the four components. The reported errors in the per-residue free energies $\Delta G_{res,i}$ and in the polar and nonpolar components of these free energies were again obtained by using standard error propagation formulas on the SEMs of the per-residue energies and of their four components calculated for each of the two states of gp17.

Generation of average structures and visualization

To assess changes in the relative positions of hydrophobic and polar residues at the domain interface upon gp17 compaction, and for visualizing these changes, we used "average" structures of gp17 in the extended and compact states. We loaded the MD simulation trajectory files (.mdcrd) and parameter files (.prmtop) into the UCSF Chimera package [45] using *MD Movie* tool and then used the *Average Structure* function to calculate the average extended- and compact-state structures from all simulated snapshots of gp17. It should be noted that the average structures were only used for determining the general locations of residues and their interactions and not for calculating exact distances between the atoms, as the averaging procedure can introduce small structural artifacts when amino acids have extensive flexibility.

Measurements of distances between charged residues

To investigate changes in ion-pairing interactions between charged groups at the interface during gp17 compaction, we monitored the distances between all pairs of charged atoms capable of forming salt bridges in the extended and compact states of gp17. In one approach, we used the function *ptraj* [46] within AmberTools to measure the fluctuations in distances between putatively interacting pairs of charged atoms during the course of the MD simulations. In another approach, we created a script that inputs the MD simulation trajectories and outputs distances between selected pairs of atoms at chosen intervals during the course of the simulation. The reported distances between pairs of charged atom were averaged over the 6400 snapshots for each of the extended- and compact-state configurations.

Measurements of vdW contacts

To investigate the vdW interaction network made by residues at the interface, we mapped out all contacts formed between each atom of the selected interface residue with all atoms from other residues within the same domain and the opposite domain. We used the *Find clashes/contacts* function in the UCSF Chimera package, with VDW-overlap parameter set to −2.75 Å to count only those pairs of interactions within the span of a single water molecule. By measuring the average number of contacts made by each residue over the simulated trajectories of the compact and extended forms of gp17, we were able to ascertain patterns of vdW contacts and how they change with gp17 compaction.

Water occupancy measurements

Some water molecules reside in stable positions throughout the simulation. Similar to water molecules that appear in X-ray crystal structures, these "bound" waters occupy positions close to the protein where they likely play a more direct role in protein function. To locate such water molecules in the extended and compact forms of gp17, we loaded trajectory files (.mdcrd) and the parameter file (.prmtop) from MD simulations of the two forms of gp17 into the *MD Movie* tool within the UCSF Chimera package. We held the gp17 molecule fixed using the *Hold steady* command and used the *Calculate Occupancy* function to calculate the fractional occupancy of water within a three-dimensional grid of volume elements defined relative to gp17 in all inputted configurations. The program outputs a pair of occupancy maps, one for the hydrogen and another one for the oxygen atoms of water around gp17. To visualize only the high-occupancy (bound) waters, we adjusted the contour levels such that only those waters present in positions more than 30% of the time were visible. We used the same procedure outlined above to obtain the water occupancy map of specific residues by holding only the selected residue fixed.

Acknowledgements

We thank Venigalla Rao, Nicholas Keller, and Tanfis Alam for discussions and experimental data on the packaging activity of wild-type and mutant T4 gp17 motor complexes. This work was supported by the National Institutes of Health grant R01-GM088186 and the National Science Foundation grant PHY-0848905 to D.E.S.

Received 8 August 2014;
Received in revised form 21 September 2014;
Accepted 26 September 2014
Available online 13 October 2014

Keywords:
molecular motors;
free energy calculations;
molecular dynamics simulations;
DNA translocation;
conformational transition

Abbreviations used:
cryo-EM, cryo-electron microscopy; vdW, van der Waals; MM-GBSA, molecular mechanics–generalized Born surface area.

References

[1] Rossmann MG, Mesyanzhinov VV, Arisaka F, Leiman PG. The bacteriophage T4 DNA injection machine. Curr Opin Struct Biol 2004;14:171–80.
[2] Hershey AD, Chase M. Independent functions of viral protein and nucleic acid in growth of bacteriophage. J Gen Physiol 1952;36:39–56.
[3] Abedon ST, Calendar RL, editors. The Bacteriophages. 2nd edit. Oxford, UK: Oxford University Press; 2006.
[4] Evilevitch A, Lavelle L, Knobler CM, Raspaud E, Gelbart WM. Osmotic pressure inhibition of DNA ejection from phage. Proc Natl Acad Sci USA 2003;100:9292–5.
[5] Smith DE, Tans SJ, Smith SB, Grimes S, Anderson DL, Bustamante C. The bacteriophage Φ29 portal motor can

package DNA against a large internal force. Nature 2001;413:748–51.
[6] Tzlil S, Kindt JT, Gelbart WM, Ben-Shaul A. Forces and pressures in DNA packaging and release from viral capsids. Biophys J 2003;84:1616–27.
[7] Purohit PK, Inamdar MM, Grayson PD, Squires TM, Kondev J, Phillips R. Forces during bacteriophage DNA packaging and ejection. Biophys J 2005;88:851–66.
[8] Harvey SC, Petrov AS, Devkota B, Boz MB. Viral assembly: a molecular modeling perspective. Phys Chem Chem Phys 2009;11:10553–64.
[9] Casjens SR. The DNA-packaging nanomotor of tailed bacteriophages. Nat Rev Microbiol 2011;9:647–57.
[10] Smith DE. Single-molecule studies of viral DNA packaging. Curr Opin Virol 2011;1:134–41.
[11] Fuller DN, Rickgauer JP, Jardine PJ, Grimes S, Anderson DL, Smith DE. Ionic effects on viral DNA packaging and portal motor function in bacteriophage Φ29. Proc Natl Acad Sci USA 2007;104:11245–50.
[12] Rickgauer JP, Fuller DN, Grimes S, Jardine PJ, Anderson DL, Smith DE. Portal motor velocity and internal force resisting viral DNA packaging in bacteriophage phi29. Biophys J 2008;94:159–67.
[13] Fuller DN, Raymer DM, Rickgauer JP, Robertson RM, Catalano CE, Anderson DL, et al. Measurements of single DNA molecule packaging dynamics in bacteriophage λ reveal high forces, high motor processivity, and capsid transformations. J Mol Biol 2007;373:1113–22.
[14] Fuller DN, Raymer DM, Kottadiel VI, Rao VB, Smith DE. Single phage T4 DNA packaging motors exhibit large force generation, high velocity, and dynamic variability. Proc Natl Acad Sci USA 2007;104:16868–73.
[15] Chemla YR, Smith DE. Single-molecule studies of viral DNA packaging in viral molecular machines. In: Rao V, Rossmann M, editors. New York, NY: Springer; 2012.
[16] Berndsen ZT, Keller N, Grimes S, Jardine PJ, Smith DE. Nonequilibrium dynamics and ultraslow relaxation of confined DNA during viral packaging. Proc Natl Acad Sci USA 2014;111:8345–50.
[17] Keller N, delToro D, Grimes S, Jardine PJ, Smith DE. Repulsive DNA–DNA interactions accelerate viral DNA packaging in phage Φ29. Phys Rev Lett 2014;112:248101.
[18] Moffitt JR, Chemla YR, Aathavan K, Grimes S, Jardine PJ, Anderson DL, et al. Intersubunit coordination in a homomeric ring ATPase. Nature 2009;457:446–50.
[19] Chistol G, Liu S, Hetherington CL, Moffitt JR, Grimes S, Jardine PJ, et al. High degree of coordination and division of labor among subunits in a homomeric ring ATPase. Cell 2012;151:1017–28.
[20] Liu S, Chistol G, Hetherington CL, Tafoya S, Aathavan K, Schnitzbauer J, et al. A viral packaging motor varies its DNA rotation and step size to preserve subunit coordination as the capsid fills. Cell 2014;157:702–13.
[21] Aathavan K, Politzer AT, Kaplan A, Moffitt JR, Chemla YR, Grimes S, et al. Substrate interactions and promiscuity in a viral DNA packaging motor. Nature 2009;461:669–73.
[22] Tsay JM, Sippy J, delToro D, Andrews BT, Draper B, Rao V, et al. Mutations altering a structurally conserved loop–helix–loop region of a viral packaging motor change DNA translocation velocity and processivity. J Biol Chem 2010;285:24282–9.
[23] Tsay JM, Sippy J, Feiss M, Smith DE. The Q motif of a viral packaging motor governs its force generation and communicates ATP recognition to DNA interaction. Proc Natl Acad Sci USA 2009;106:14355–60.
[24] Feiss M, Rao VB. In: Rao VB, Rossmann M, editors. he bacteriophage DNA packaging machine in viral molecular machines. New York, NY: Springer; 2012.
[25] Sun S, Kondabagil K, Draper B, Alam TI, Bowman VD, Zhang Z, et al. The structure of the phage T4 DNA packaging motor suggests a mechanism dependent on electrostatic forces. Cell 2008;135:1251–62.
[26] Sun S, Kondabagil K, Gentz PM, Rossmann MG, Rao VB. The structure of the ATPase that powers DNA packaging into bacteriophage T4 procapsids. Mol Cell 2007;25:943–9.
[27] Dixit AB, Ray K, Thomas JA, Black LW. The C-terminal domain of the bacteriophage T4 terminase docks on the prohead portal clip region during DNA packaging. Virology 2013;446:293–302.
[28] Hegde S, Padilla-Sanchez V, Draper B, Rao VB. Portal-large terminase interactions of the bacteriophage T4 DNA packaging machine implicate a molecular lever mechanism for coupling ATPase to DNA translocation. J Virol 2012;86:4046–57.
[29] Migliori AD, Keller N, Alam TI, Mahalingam M, Rao VB, Arya G, et al. Evidence for an electrostatic mechanism of force generation by the bacteriophage T4 DNA packaging motor. Nat Commun 2014;5:4173.
[30] Massova I, Kollman PA. Combined molecular mechanical and continuum solvent approach (MM-PBSA/GBSA) to predict ligand binding. Perspect Drug Discov 2000;18:113–35.
[31] Lee KK, Fitch CA, García-Moreno EB. Distance dependence and salt sensitivity of pairwise, coulombic interactions in a protein. Protein Sci 2002;11:1004–16.
[32] Kumar S, Nussinov R. Relationship between ion pair geometries and electrostatic strengths in proteins. Biophys J 2002;83:1595–612.
[33] Kumar S, Nussinov R. Close-range electrostatic interactions in proteins. ChemBioChem 2002;3:604–17.
[34] Fu H, Grimsley GR, Razvi A, Scholtz JM, Pace CN. Increasing protein stability by improving beta-turns. Proteins 2009;77:491–8.
[35] Fischer S. From the cover: structural mechanism of the recovery stroke in the myosin molecular motor. Proc Natl Acad Sci USA 2005;102:6873–8.
[36] Aksimentiev A, Balabin IA, Fillingame RH, Schulten K. Insights into the molecular mechanism of rotation in the Fo sector of ATP synthase. Biophys J 2004;86:1332–44.
[37] Humphrey W, Andrew D, Schulten K. VMD: visual molecular dynamics. J Mol Graphics 1996;14:33–8.
[38] Phillips JC, Braun R, Wang W, Gumbart J, Tajkhorshid E, Villa E, et al. Scalable molecular dynamics with NAMD. J Comput Chem 2005;26:1781–802.
[39] Foloppe N, MacKerell AD. All-atom empirical force field for nucleic acids: I. Parameter optimization based on small molecule and condensed phase macromolecular target data. J Comput Chem 2000;21:86–104.
[40] Yang D, Arya G. Structure and binding of the H4 histone tail and the effects of lysine 16 acetylation. Phys Chem Chem Phys 2011;13:2911–21.
[41] Pearlman DA, Case DA, Caldwell JW, Ross WS, Cheatham TE, DeBolt S, et al. AMBER, a package of computer programs for applying molecular mechanics, normal mode analysis, molecular dynamics and free energy calculations to simulate the structural and energetic properties of molecules. Comput Phys Commun 1995;91:1–41.

[42] Srinivasan J, Trevathan MW, Beroza P, Case DA. Application of a pairwise generalized Born model to proteins and nucleic acids: inclusion of salt effects. Theor Chem Acc 1999; 101:426–34.
[43] Hinsen K. The molecular modeling toolkit: a new approach to molecular simulations. J Comput Chem 2000;21:79–85.
[44] Zoete V, Meuwly M, Karplus M. Study of the insulin dimerization: binding free energy calculations and per-residue free energy decomposition. Proteins 2005;61:79–93.
[45] Pettersen EF, Goddard TD, Huang CC, Couch GS, Greenblatt DM, Meng EC, et al. UCSF Chimera—a visualization system for exploratory research and analysis. J Comput Chem 2004;25:1605–12.
[46] Roe DR, Cheatham TE. PTRAJ and CPPTRAJ: software for processing and analysis of molecular dynamics trajectory data. J Chem Theory Comput 2013;9:3084–95.